Operating slip modes and inhomogeneous plastic deformation of Mg−10Gd−3Y−0.5Zr alloy during compression

Zhi-wei JIANG[1], Dong-di YIN[1], You-fu WAN[1], Ran NI[1], Hao ZHOU[2], Jiang ZHENG[3], Qu-dong WANG[4]

1. Key Laboratory of Advanced Technologies of Materials, Ministry of Education,
School of Materials Science and Engineering, Southwest Jiaotong University, Chengdu 610031, China;
2. Nano and Heterogeneous Materials Center, School of Materials Science and Engineering,
Nanjing University of Science and Technology, Nanjing 210094, China;
3. Shenyang National Laboratory for Materials Science,
International Joint Laboratory for Light Alloys (Ministry of Education),
College of Materials Science and Engineering, Chongqing University, Chongqing 400044, China;
4. National Engineering Research Center of Light Alloys Net Forming,
School of Materials Science and Engineering, Shanghai Jiao Tong University, Shanghai 200240, China

Abstract: To understand the operating slip modes and inhomogeneous plastic deformation quantitatively and statistically for a high-performance cast Mg−10Gd−3Y−0.5Zr (wt.%, GW103) alloy during room-temperature uniaxial compression, detailed slip trace analysis and electron backscatter diffraction (EBSD) based misorientation analysis of this alloy in aged condition were carried out. After 2% plastic strain, according to relative frequency of identified slip traces, the active slip modes were basal $\langle a \rangle$ slip (73.3%), followed by prismatic $\langle a \rangle$ slip (15.8%), then second-order pyramidal $\langle c+a \rangle$ slip (6.9%), and finally first-order pyramidal $\langle a \rangle$ slip (4%). Although most of the active slip systems exhibited large Schmid factor (m) values (>0.3), it was worth noting that some hard-oriented ($m<0.1$) slip systems were also active. For most of the grain boundaries exhibiting extremely large geometrically necessary dislocation (GND) density, at least one of the following conditions was satisfied: large grain boundary misorientation angle (GBMA) and/or large deviation of m_{max} for particular slip mode between neighboring grains. The plastic heterogeneity of grains (magnitude/distribution of GND density) was independent of the visibility of slip traces. The grain orientation speared (GOS) and/or grain average GND density showed no obvious correlation with m_{max} (for particular slip mode).

Key words: Mg−RE alloy; operating slip mode; slip trace analysis; plastic deformation heterogeneity; geometrically necessary dislocation (GND) density

1 Introduction

As the lightest metal structural material, magnesium (Mg) alloy has great demand potential in the transportation field [1−5]. However, conventional Mg alloys have low ductility and/or strength [6−8]. Rare-earth element alloying was an available solution to simultaneously enhance the ductility and strength of Mg [9], which was

attributed to the excellent texture weakening [10], solid solution strengthening [11], precipitation strengthening [12], and more importantly, enhanced non-basal slip activity [13]. Mg alloys with Gd and Y added showed high strength at both room-temperature (RT) and high temperature [14] and good creep resistance [15,16]. In particular, by optimizing the parameters of heat treatment, HE et al [12] developed high-strength cast Mg−10Gd−3Y−0.5Zr (wt.%, thereafter, unless otherwise

specified, the mass fraction is used to indicate the alloy composition, GW103) Mg alloys at RT.

The activated deformation mechanism determined the mechanical behavior of the material. Therefore, understanding the active slip mode was very necessary, especially at the statistical perspective [17]. Mg and its alloys have close-packed hexagonal crystal structure with low symmetry characteristics [18]. In addition, the significant differences in the activated slip modes during the deformation process hindered the further application of Mg alloys [6,19,20]. Generally, at RT, for slip-dominated plastic deformation process, since the critical resolved shear stress (CRSS) of basal $\langle a \rangle$ slip was the smallest in various slip modes [21,22], the relative frequency of basal $\langle a \rangle$ slip usually was the largest. In Mg alloys, the activated non-basal slip was one of the critical roles for the yield strength and strain-hardening behavior of the material [23], even if the basal $\langle a \rangle$ slip was the most likely activated slip mode. For example, the pyramidal $\langle c+a \rangle$ slip that can satisfy the von Mises criterion and coordinate the c-axis strain of the crystal was rarely activated [24].

WANG et al [25] systematically studied the activation of the deformation mechanism of the extruded GW103 alloy at high temperature during uniaxial tension, and found that the activation ratio of non-basal slip decreased with increasing temperature. For the extruded and cast GW103 alloy, a significant difference in the activation of the deformation mechanism during high temperature uniaxial tensile deformation was found [26]. What's more, in cast Mg alloys with random texture, tension−compression asymmetry has also been found [27,28]. Therefore, the quantitative activation of the deformation mechanism during uniaxial compression deformation of cast GW103 alloy at RT needs further study.

For the mechanical behavior of Mg alloys, the evolution of plastic heterogeneity can provide new insights. To coordinate the plastic deformation, the adjacent grains and/or regions will usually deform coordinately, and the plastic heterogeneity may develop in the microstructure [29]. The plastic deformation is able to cause displacement/strain and lattice rotation in the crystal [30,31], so plastic heterogeneity can be characterized by local strain [32,33] and/or local misorientation [29,34]. For instance, for Mg−1.3Zn−0.25Zr−0.20Nd [35],

there was a significant difference between the local strain and the macroscopic strain based on digital image correlation (DIC) measurement. CHAI et al [36] found inhomogeneous intragranular misorientation angle (IGM) and geometrically necessary dislocation (GND) density in pure Mg, which was based on electron backscatter diffraction (EBSD) analysis. The understanding of plastic heterogeneity is still insufficient in Mg alloys, and even some studies on plastic heterogeneity have been conducted [37−39].

The purpose of this work is to study the operating slip modes and inhomogeneous plastic deformation quantitatively and statistically for a high-performance cast GW103 alloy during RT uniaxial compression. To achieve this, a detailed quasi-in-situ grain-by-grain slip trace analysis and EBSD based misorientation analysis were performed on the grain/sub-grain scale. In addition, the factors that may affect the inhomogeneous plastic deformation of IGM and GND density were investigated, including slip activity and grain orientation. This work provides new insights into the plastic deformation behavior and provides guidance for the plastic deformation modeling of Mg alloys.

2 Experimental

The cast Mg−10Gd−3Y−0.5Zr alloy was used in this study. By melting in a mild steel crucible at about 750 °C, the GW103 alloy was prepared from Mg (99.95%) with high purity and master alloys of Mg−25Gd, Mg−25Y and Mg−30Zr. Mg−9.87Gd−2.9Y−0.39Zr was the actual chemical composition of the GW103 alloy, which was measured by an inductively coupled plasma (ICP) analyzer. For the heat treatment process of the material, the material was solution treated at 500 °C for 6 h at first, and then aged at 225 °C for 3 h [12,14].

By means of electric spark machining, the compressive samples were cut from the cast ingot. For the cuboid compressive samples, with dimensions of 7.5 mm (length) × 5 mm (width) × 5 mm (thickness) [40], the length, width and thickness are along the reference direction (RD), the transverse direction (TD) and the normal direction (ND), respectively. The uniaxial compression experiment with an initial strain rate of 0.001 s^{-1} in which the loading direction was parallel to the RD,

was conducted on the universal testing machine (MTS−CMT5105). To ensure repeatability and accuracy, the compressive tests were repeated no less than three times. Besides, to reduce the compliance problems caused by the machine, the plastic strain was calculated by subtracting the elastic deformation from the total deformation during the measurement [41,42]. Then, the engineering stress−engineering plastic strain curve was obtained. After that, true stress−true plastic strain was obtained based on engineering stress− engineering plastic strain, which was applied in this study unless otherwise stated. The yield strength was specified as the 0.2% proof stress. The strain hardening rate (θ) was calculated by [43]

$$\theta = \frac{\mathrm{d}\sigma}{\mathrm{d}\varepsilon} \qquad (1)$$

where σ and ε are true stress and true plastic strain, respectively.

For the characterization of the microstructure of the material, the Zeiss Axio Lab A1 optical microscope (OM) and the FEI Quanta 250 FEG and/or JEOL JSM−7800F scanning electron micro-scope (SEM) were used. The crystallographic orientation of the material was obtained by the Oxford Instrument Nordlys Nano EBSD detector. The observation surface was a plane composed of RD and TD. For all the specimens for micro-structure characterization, they were ground down to 3000# SiC paper. Next, the mechanical polishing process was applied to the surface for observation. Then, the chemical polishing was conducted for 1−2 s. The polishing solutions were made by mixing 2.3 mL nitric acid, 6.6 mL hydrochloric acid and 20 mL ethanol. Finally, the sample was etched in nitric acid aqueous solution (10 vol.%) for 1 s.

In this study, to study the evolution of the surface microstructure during the deformation process, 2% plastic strain (ε_{p2}) was selected to interrupt the test. The surface of the sample in the same area was observed by secondary electron (SE) SEM and/or EBSD (the area is located in the center of the sample surface). Before loading, the sample was subjected to the above polishing step. At least 250 grains were contained in the observation area. The scanning step size was 2 μm in the acquisition process of EBSD. As far as the indexing ratio of average EBSD was concerned, it was above 90%. For grain reconstruction, 10° was adopted as the

critical grain boundary misorientation angle (GBMA). The homemade MATLAB code (derived from the open-source toolbox MTEX), was applied to the analysis of EBSD data [44,45].

While tracking the same area, the slip traces occurring in the grains should be paid special attention. The slip trace analysis technique was applied to analyzing the activated slip systems. For the active slip systems, they were regarded as the theoretical slip trace which had the best matching relationship with the observed slip trace. Using the mean orientation of the grains collected by EBSD, the homemade MATLAB code was applied to calculating the theoretical slip traces. More details of this analytical technique were shown in the previous works [21,25,41,46−48].

Inhomogeneous plastic deformation with regard to misorientation was investigated utilizing a MTEX-based house-made MATLAB script [44,45]. IGM was calculated as the misorientation angle between the studied pixel and the mean orientations of the grains inside a grain [39,44,45,47], thereby being induced to assess long-range orientation gradients [36,46,47]. Based on Nye's model, GND density was calculated with MTEX [38,44,45,49]. Under the assumption that all dislocation systems had equivalent line energy, the GND density lower-bound was derived [50]. A total of 27 dislocation systems (Table 1), according to the identified slip systems in this study, were considered in the calculation of GND density. In addition, grain orientation speared (GOS) and grain average GND density (gGND density) were calculated as the average IGM and GND density inside one grain, respectively [46].

3 Results

3.1 Initial microstructure

The representative microstructure of the GW103 alloy, IPF maps, the corresponding EBSD maps and equivalent grain diameter distribution are shown in Fig. 1. The microstructure of the alloy consisted of equiaxed α-Mg grains and secondary phase particles. Based on previous studies [12,25], the secondary phase particles were mainly cuboid-shaped phases rich in Gd and Y, and had an fcc structure. From Fig. 1(c), the grain size showed a uniform distribution. The average equivalent grain size was (75±36) μm. The pole figure and inverse

Table 1 Dislocation systems considered in GND density calculations

Dislocation	ID	Burgers vector	Line vector
	1	$[2\bar{1}\bar{1}0]$	$[0\bar{1}10]$
	2	$[\bar{1}2\bar{1}0]$	$[10\bar{1}0]$
	3	$[\bar{1}\bar{1}20]$	$[\bar{1}100]$
	4	$[2\bar{1}\bar{1}0]$	$[000\bar{1}]$
	5	$[\bar{1}2\bar{1}0]$	$[000\bar{1}]$
	6	$[\bar{1}\bar{1}20]$	$[000\bar{1}]$
	7	$[\bar{2}113]$	$[01\bar{1}0]$
	8	$[\bar{1}\bar{1}23]$	$[\bar{1}100]$
	9	$[1\bar{2}13]$	$[\bar{1}010]$
Edge	10	$[2\bar{1}\bar{1}3]$	$[0\bar{1}10]$
	11	$[11\bar{2}3]$	$[1\bar{1}00]$
	12	$[\bar{1}2\bar{1}3]$	$[10\bar{1}0]$
	13	$[\bar{1}2\bar{1}0]$	$[10\bar{1}2]$
	14	$[\bar{2}110]$	$[01\bar{1}2]$
	15	$[\bar{1}\bar{1}20]$	$[\bar{1}10\bar{2}]$
	16	$[1\bar{2}10]$	$[\bar{1}01\bar{2}]$
	17	$[2\bar{1}\bar{1}0]$	$[0\bar{1}1\bar{2}]$
	18	$[11\bar{2}0]$	$[1\bar{1}0\bar{2}]$
	1	$[2\bar{1}\bar{1}0]$	
	2	$[\bar{1}2\bar{1}0]$	
	3	$[\bar{1}\bar{1}20]$	
	4	$[\bar{2}113]$	
Screw	5	$[\bar{1}\bar{1}23]$	
	6	$[1\bar{2}13]$	
	7	$[2\bar{1}\bar{1}3]$	
	8	$[11\bar{2}3]$	
	9	$[\bar{1}2\bar{1}3]$	

Fig. 1 Representative initial microstructures of GW103 alloy on RD−TD plane: (a) Optical micrograph; (b) IPF map for RD−TD plane; (c) Equivalent grain diameter distribution based on EBSD; (d) Corresponding {0001} PF and IPF along RD

pole figure showed that the grain orientation of the alloy was randomly distributed.

3.2 Mechanical behavior

As can be seen from the true stress−true plastic strain curve of the GW103 alloy (Fig. 2(a)), the yield strength (YS), ultimate strength (US) and uniform elongation (UEL) of the material were (227 ± 13) MPa, (415 ± 23) MPa and 0.19 ± 0.01, respectively. It is manifest from the strain hardening behavior during compression deformation (Fig. 2(b)) that the alloy showed the characteristics of slip-dominated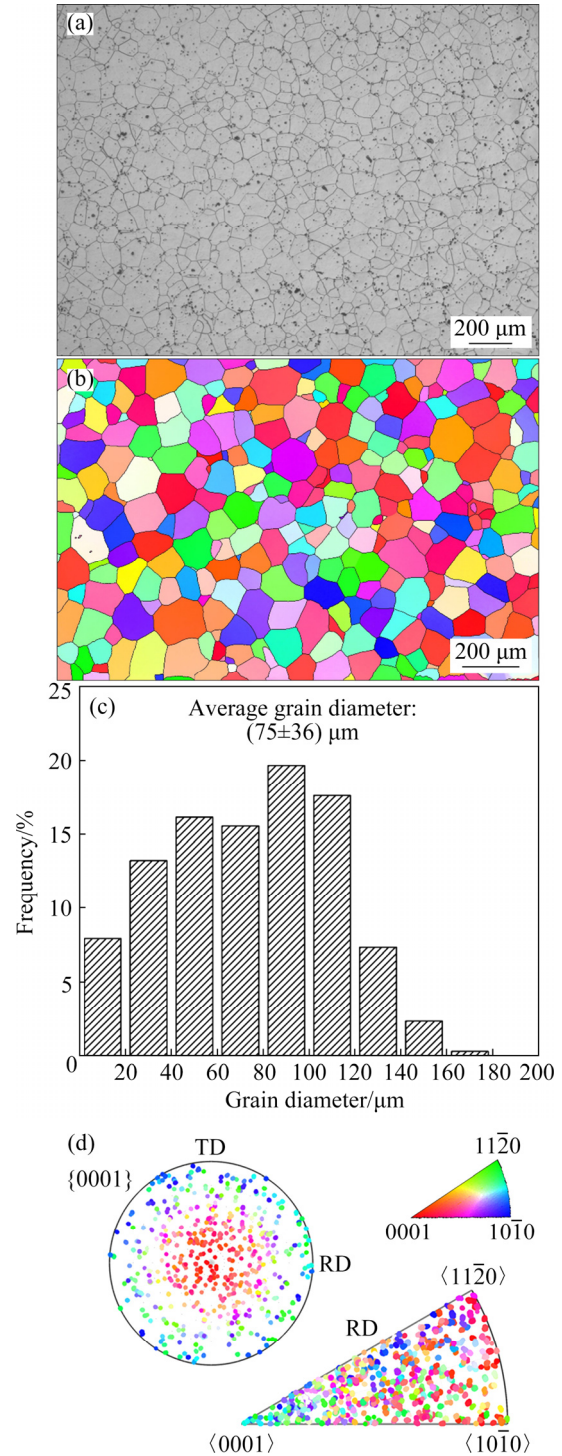 deformation [51]. During compression deformation, the strain hardening rate sharply decreased due to the elastoplastic transition. Then, the strain hardening rate showed a slower linear decrease due to the dynamic recovery at higher stress levels.
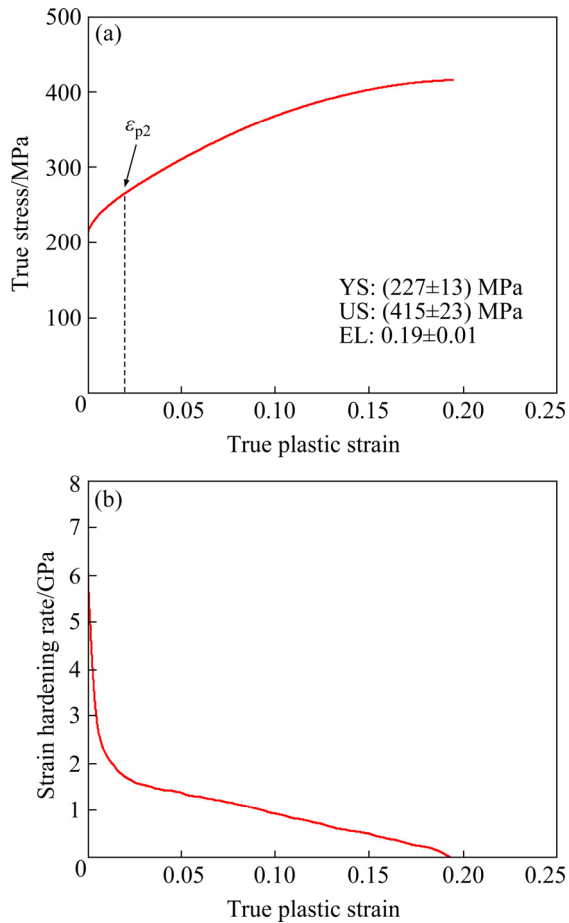
Fig. 2 Mechanical behavior curves of GW103 alloy: (a) True stress−true plastic strain curve along RD; (b) Corresponding strain hardening rate−true plastic strain curve

3.3 Slip activity

To further explore the activation of the deformation mechanism during plastic deformation in the GW103 alloy, the quasi-in-situ experiment of compression was performed. By tracking the same area of the sample surface (the area is located in the center of the sample surface), the evolution of the microstructure was detailedly studied (with particular attention to the observed slip trace).

The evolution of the microstructure in the same area during the quasi-in-situ compression test is shown in Fig. 3. At ε_{p2} deformation stage, slip traces were clearly observed. However, no twins were clearly observed. Therefore, the observed slip trace was analyzed in detail. Most slip traces exhibited typical planar slip characteristics [41]. For most grains with observed slip traces, in one grain, only one series of parallel slip traces was observed. This indicated that single slip dominated the deformation. It should be noted that a total of 8

areas were tracked and studied in the present work, which contained a total of 293 grains, and all of them exhibited similar evolution, thus only one area was provided here.

Figure 4 shows the frequency of all grains which exhibited slip trace and no slip trace in the study area. The number of grains was given in parentheses. Among all grains analyzed, about 31%
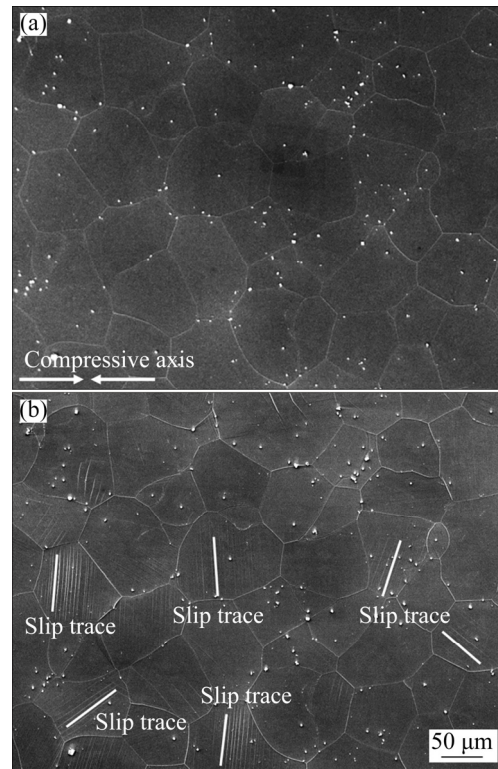

Fig. 3 SE SEM micrographs of representative microstructure evolution during quasi-in-situ compression deformation: (a) Before loading; (b) At ε_{p2} deformation stage (The slip traces are marked by white lines)
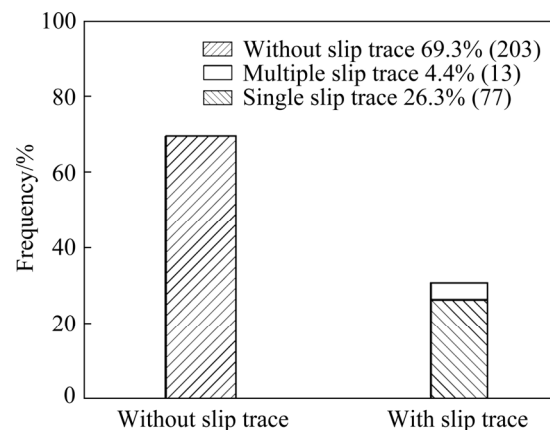

Fig. 4 Frequency of all grains exhibiting slip trace and no slip trace (The number of grains is written in parentheses)

of grains with slip trace were observed. For the grains where slip trace was observed, the single slip was observed in about 86% of the grains.

The slip trace analysis technique was used to identify the observed slip trace grain by grain to further identify the activated slip system [48]. Four slip modes (with 18 slip systems) in the Mg alloys were considered in this study. The slip modes were basal $\langle a \rangle$ slip (Bas $\langle a \rangle$, $\{0001\}\langle 11\bar{2}0 \rangle$), prismatic $\langle a \rangle$ slip (Pri $\langle a \rangle$, $\{10\bar{1}0\}\langle 11\bar{2}0 \rangle$), second-order pyramidal $\langle c+a \rangle$ slip (Pyr II $\langle c+a \rangle$, $\{11\bar{2}2\}$-$\langle \bar{1}\bar{1}23 \rangle$), and first-order pyramidal $\langle a \rangle$ slip (Pyr I $\langle a \rangle$, $\{10\bar{1}1\}\langle 11\bar{2}0 \rangle$). According to the literatures [25,41,48,51,52], the corresponding slip system information is summarized in Table 2.

An example of the grain with slip trace is shown in Fig. 5(a). Moreover, the example of using the slip trace analysis technique is also shown in Fig. 5. The sample was compressed to the ε_{p2} deformation stage. Two sets of slip traces were observed in No. 110 grain (Fig. 5(a)) through SE SEM micrographs. The grain mean orientation of No. 110 grain before loading was obtained by EBSD (Fig. 5(b)). Using the homemade MATLAB code, the possible slip traces and the orientation of the HCP unit cell were calculated. According to the matching results of the observed slip trace and

Table 2 All slip systems considered in slip trace analysis

No.	Mode	Slip system
1		$(0001)[2\bar{1}\bar{1}0]$
2	Basal $\langle a \rangle$ (Bas $\langle a \rangle$)	$(0001)[\bar{1}2\bar{1}0]$
3		$(0001)[\bar{1}\bar{1}20]$
4		$(01\bar{1}0)[2\bar{1}\bar{1}0]$
5	Prismatic $\langle a \rangle$ (Pri $\langle a \rangle$)	$(10\bar{1}0)[\bar{1}2\bar{1}0]$
6		$(\bar{1}100)[\bar{1}\bar{1}20]$
7		$(2\bar{1}\bar{1}2)[\bar{2}113]$
8		$(11\bar{2}2)[\bar{1}\bar{1}23]$
9	Second-order pyramidal	$(\bar{1}2\bar{1}2)[1\bar{2}13]$
10	$\langle c+a \rangle$ (Pyr II $\langle c+a \rangle$)	$(\bar{2}112)[2\bar{1}\bar{1}3]$
11		$(\bar{1}\bar{1}22)[11\bar{2}3]$
12		$(1\bar{2}12)[\bar{1}2\bar{1}3]$
13		$(10\bar{1}1)[\bar{1}2\bar{1}0]$
14		$(01\bar{1}1)[\bar{2}110]$
15	First-order pyramidal	$(\bar{1}101)[\bar{1}\bar{1}20]$
16	$\langle a \rangle$ (Pyr I $\langle a \rangle$)	$(\bar{1}011)[1\bar{2}10]$
17		$(0\bar{1}11)[2\bar{1}\bar{1}0]$
18		$(1\bar{1}01)[11\bar{2}0]$

theoretical slip trace, the slip system 6 (the slip plane was $(\bar{1}100)$, the slip direction was $[\bar{1}\bar{1}20]$, the Schmid factor (m) was 0.45, and the deviation
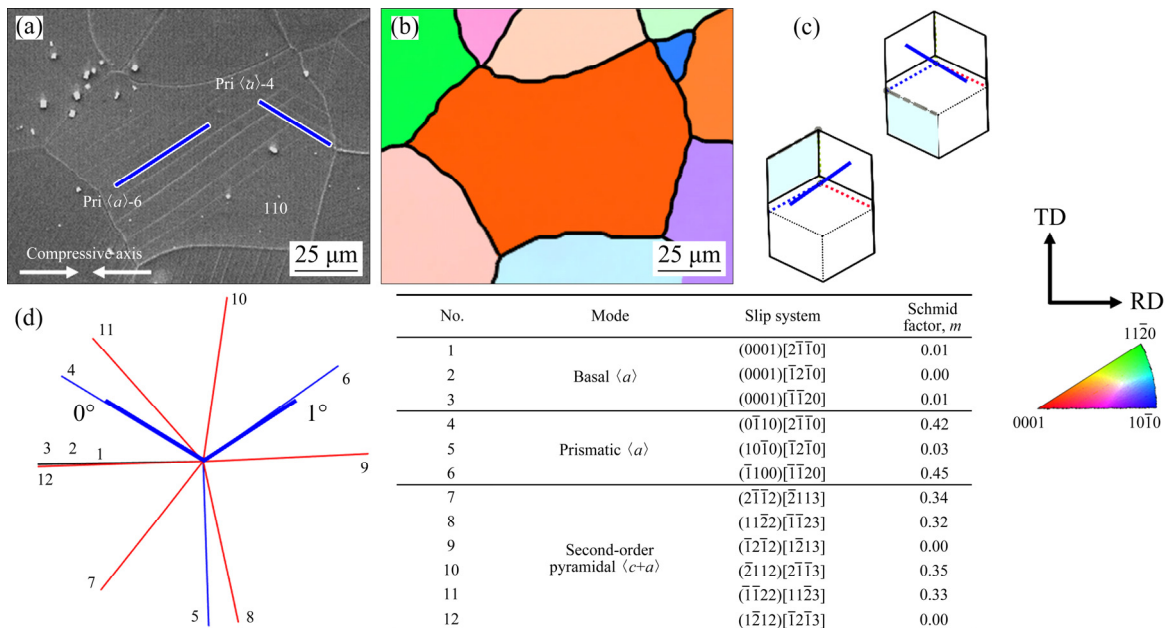

No.	Mode	Slip system	Schmid factor, m
1		$(0001)[2\bar{1}\bar{1}0]$	0.01
2	Basal $\langle a \rangle$	$(0001)[\bar{1}2\bar{1}0]$	0.00
3		$(0001)[\bar{1}\bar{1}20]$	0.01
4		$(0\bar{1}10)[2\bar{1}\bar{1}0]$	0.42
5	Prismatic $\langle a \rangle$	$(10\bar{1}0)[\bar{1}2\bar{1}0]$	0.03
6		$(\bar{1}100)[\bar{1}\bar{1}20]$	0.45
7		$(2\bar{1}\bar{1}2)[\bar{2}113]$	0.34
8		$(11\bar{2}2)[\bar{1}\bar{1}23]$	0.32
9	Second-order	$(\bar{1}2\bar{1}2)[1\bar{2}13]$	0.00
10	pyramidal $\langle c+a \rangle$	$(\bar{2}112)[2\bar{1}\bar{1}3]$	0.35
11		$(\bar{1}\bar{1}22)[11\bar{2}3]$	0.33
12		$(1\bar{2}12)[\bar{1}2\bar{1}3]$	0.00

Fig. 5 Slip trace analysis results of grain No. 110 of GW103 alloy at ε_{p2} deformation stage: (a) SE SEM photo-micrograph; (b) Corresponding IPF map; (c) Unit cell visualizing grain orientation and identified active slip systems; (d) Calculated slip traces for all possible slip systems (12 most common slip systems are shown here) (The inserted table shows the details of the possible slip systems and the corresponding m)

angle was 1°) and the slip system 4 (the slip plane was $(01\bar{1}0)$, the slip direction was $[2\bar{1}\bar{1}0]$, the m was 0.42, and the deviation angle was 0°) were selected as reasonable active slip systems, respectively.

The slip systems and operating slip modes were identified on about 293 grains by using the slip trace analysis technique. Most active slip systems can be identified by different slip traces and the smallest deviation angles. The deviation angle was considered to be the deviation angle between the observed slip trace and the best-matching slip traces. For some slip systems (with the same slip plane, for example, all Bas $\langle a \rangle$ slips), if the slip system was involved in cross slip, it can be identified by the feature (the same Burgers vector). Otherwise, the slip trace cannot be accurately identified by slip trace analysis. In this case, for Bas $\langle a \rangle$ slip, the slip system with the largest m was considered to be active [21].

Figure 6 summarizes the m distributions as well as frequency of the identified slip traces (all the 101 series of slip traces) for particular slip modes during compression deformation. The number in parentheses indicates all of slip traces. At the ε_{p2} deformation stage, the deformation was dominated by Bas $\langle a \rangle$ slip (73.3%). The activation of the other slip modes was 15.8% Pri $\langle a \rangle$ slip, 6.9% Pyr II $\langle c+a \rangle$ slip, and 4% Pyr I $\langle a \rangle$ slip. Among them, the relative frequency of Bas $\langle a \rangle$ slip and Pri $\langle a \rangle$ slip in the larger m ($m>0.3$) interval were 68.9% and 88.0%, respectively. However, the m distribution of Pyr II $\langle c+a \rangle$ slip and Pyr I $\langle a \rangle$ slip was random, which may be related to the lack of
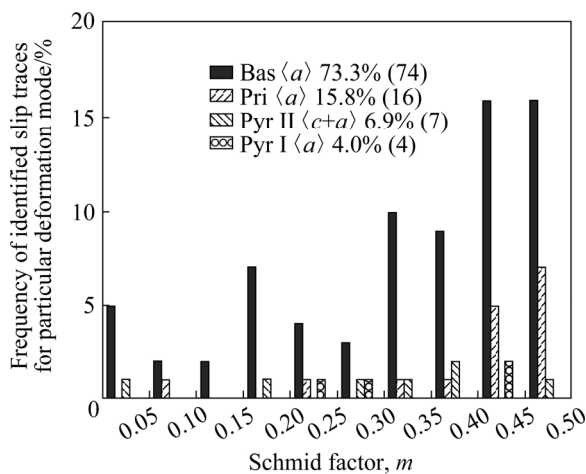
statistics. It was worth noting that some hard-oriented ($m<0.1$) slip systems were also activated.

Figure 7 shows deviation angle distributions of all the identified slip traces and the best-matching slip traces. For the deviation angles, all of them were within 6°, and most (~87%) of them were lower than 4°. This was reasonable and acceptable for the small deviations caused by lattice rotation (it may be caused by deformation) and the misalignment in the SEM and/or EBSD tests.
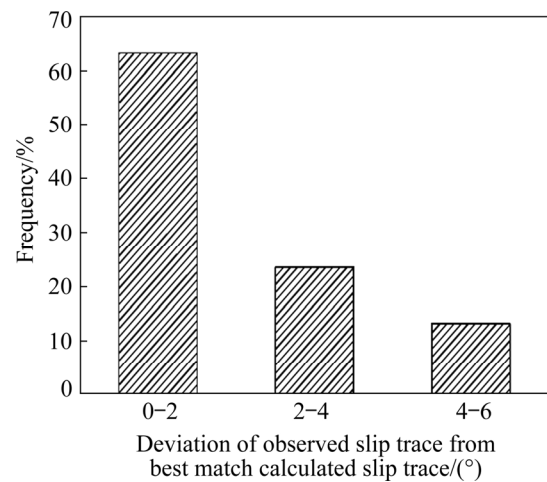

Fig. 7 Deviation angle distributions of all identified slip traces and best-matching slip traces for all 101 series of slip traces

3.4 Plastic heterogeneity

The gradient of plastic strain leads to the generation of misorientation of the crystal lattice, and the parameters based on the misorientation were usually used to characterize the degree of plastic heterogeneity [53]. The IGM is a parameter that characterizes the long-range deformation heterogeneity inside a grain, and the IGM for a pixel in this study is defined as the angle of misorientation between the pixel orientation and the mean orientations of the grains [46,47]. In addition, the GND is an essential dislocation, which is generated to coordinate the different strains and orientations of adjacent regions in heterogeneous deformation [47,54]. This is another important parameter for evaluating plastic heterogeneity. Therefore, in this work, both parameters above were investigated.

Figure 8 shows the IGM maps of the same area before loading and at ε_{p2} deformation stage. Before loading, the IGM was small and exhibited a relatively uniform distribution for most grains.

Fig. 6 Stacked map of m distributions for all activated slip modes at ε_{p2} deformation stage (The number of slip traces is written in parentheses)

However, at ε_{p2} deformation stage, the magnitude of IGM was greatly increased, and the distribution of IGM became more inhomogeneous, especially at the vicinity of grain boundaries (GBs). There were also some areas with large IGM in grain interior, despite it being much weaker than that near GBs. The average IGM of the entire studied area increased from 0.26° to 0.58° (by 123%). This indicated that plastic heterogeneity was enhanced by the deformation.
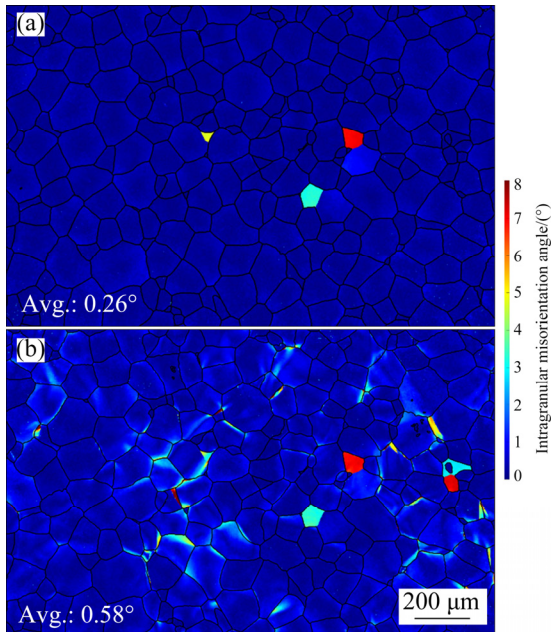

Fig. 9 Statistical distributions of IGM before loading and at ε_{p2} deformation stage

Fig. 8 IGM maps of same area for different deformation stages: (a) Before loading; (b) At ε_{p2} deformation stage

The statistical distributions of IGM before loading and at ε_{p2} deformation stage are provided in Fig. 9. At the ε_{p2} deformation stage, the magnitude of IGM increased and its distribution became more scattered after deformation, which was consistent with the spatial distributions. For example, before loading, the largest peak of the IGM distribution was in the interval of 0.16−0.24, and over 95% of IGM was lower than 0.5°. After deformation, IGM became larger, and only about 60% of IGM was lower than 0.5°.

Figure 10 shows the GND density maps of the same area before loading and at ε_{p2} deformation stage. Generally, the spatial distribution trends of the GND density were similar to those of the IGM. However, the GND density maps revealed more details of the inhomogeneous deformation. Before loading, the GND density was small and exhibited a uniform distribution for most grains. However, at
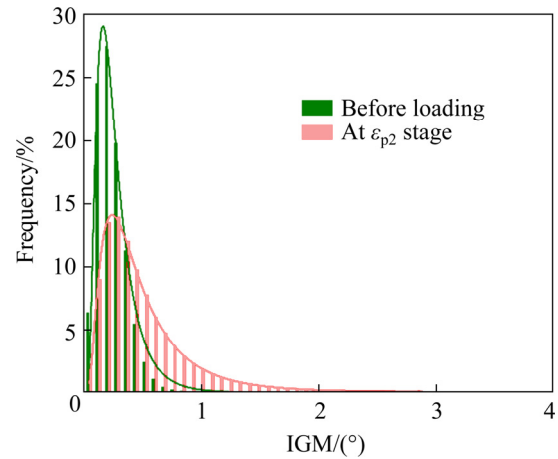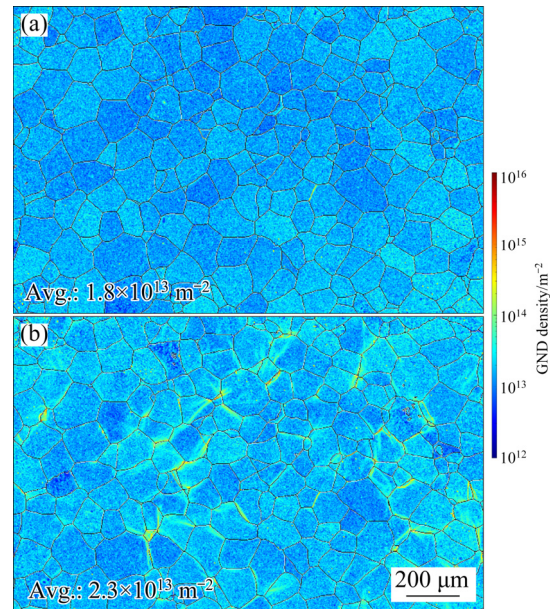

Fig. 10 GND density maps of same area for different deformation stages: (a) Before loading; (b) At ε_{p2} deformation stage

ε_{p2} deformation stage, the magnitude of GND density was greatly increased, and the distribution of GND density became more inhomogeneous, especially at the vicinity of GBs. It was worth noting that there were also some areas with large GND density in grain interior. The average GND density of the entire studied area increased from 1.8×10^{13} to 2.3×10^{13} m^{-2} (by 31%). This indicated that plastic heterogeneity was enhanced by the deformation.

The statistical distributions of GND density before loading and at ε_{p2} deformation stage are provided in Fig. 11. Compared with those before loading, the GND density increased and its

distribution became more scattered after the deformation, which was consistent with the spatial distributions. Interestingly, for the IGM and the GND density, all the quantities before loading and after the deformation approximately followed a lognormal distribution, which was also found in metals including other Mg alloys [38,46,54].
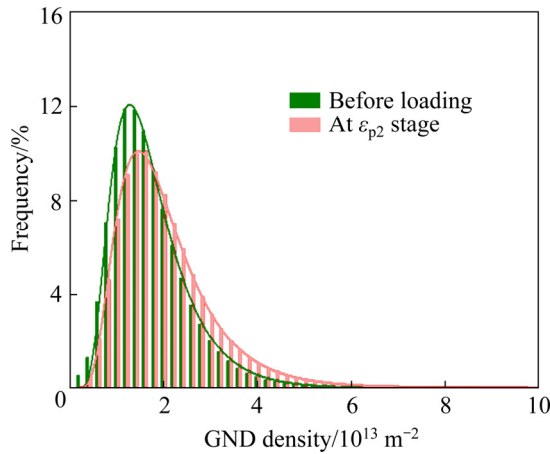

Fig. 11 Statistical distributions of GND density before loading and at ε_{p2} deformation stage

4 Discussion

4.1 Effects of precipitate on slip activity

For aged Mg−rare-earth alloys, the precipitates were considered to be one of the key roles of high strength [46], especially the prismatic precipitates [55,56]. NI et al [46] conducted a quantitative study on the deformation mechanism of the cast Mg−11Y−5Gd−2Zn−0.5Zr alloy during compression at RT. After the peak-aged treatment, the relative frequency of Pyr II $\langle c+a \rangle$ slip, which was originally the dominant slip mode, was reduced from 34.1% to 27.8%. The relative frequency of Bas $\langle a \rangle$ slip increased from 29.8% to 50.5%, becoming the dominant slip system. As shown in Section 3.4, the dominant slip mode of the alloy studied in this work was Bas $\langle a \rangle$ slip (the relative frequency was 73.3%). It was worth noting that the relative frequency of Pyr II $\langle c+a \rangle$ slip was only 6.9%. For the extruded Mg−1Mn−0.7Nd (MN11) alloy [17], in the compression deformation at RT, after aging, the dominant slip mode was still the Bas $\langle a \rangle$ slip (the relative frequency exceeded 70%). For the extruded MN11 alloy [17], for samples with different precipitate contents during compression deformation at 250 °C, as the precipitate content increased, the dominant slip mode did not change,

which was the Bas $\langle a \rangle$ slip. However, the relative frequency of Bas $\langle a \rangle$ slip was first reduced and then increased. Regardless of the presence of texture, the precipitate significantly affects the relative activity of individual slip systems. Therefore, the effects of precipitate relative to individual slip mode need further study.

It is worth noting that tension−compression asymmetry generally exists in Mg alloys [41]. It is generally considered to be affected by texture and twin. Generally, solid solution and precipitates were considered to be the key roles in the tension−compression asymmetry of Mg alloys [41,57]. For example, YIN et al [41] found that the tension−compression asymmetry of Mg−0.5Y and Mg−5Y showed the opposite behavior. The study on extruded MN11 alloy [17] found that, after aging, during tension and compression deformation at RT, the dominant slip mode did not change, which was the Bas $\langle a \rangle$ slip. However, during the tension deformation, the relative proportion of the Bas $\langle a \rangle$ slip gradually decreases, while it remains basically unchanged during the compression deformation. Therefore, considering the complex relationship between the tension−compression asymmetry and the deformation mechanism, the effects of the precipitate relative to individual slip mode under different deformation conditions also need to be further studied.

4.2 Development of plastic heterogeneity

According to the results in Section 3.4, for the spatial distribution and statistical information of IGM and GND density, at ε_{p2} deformation stage, obvious plastic deformation heterogeneity is already shown on the grain-scale. It is worthwhile to explore the relationship between plastic heterogeneity and deformation-related characteristics/parameters, including slip trace, grain size, large grain boundary misorientation angle (GBMA) and m, etc.

Figure 12 provides some examples of the GND density of the grains with and without observable slip traces. The active slip system in Grain 203 (Fig. 12(a)) was identified as Bas $\langle a \rangle$ $((0001)[\bar{1}2\bar{1}0])$ slip, with large m (0.36). The GND density was almost unchanged before loading and after deformation, although slip traces were clearly observed in the grain. On the contrary, slip traces appeared in the upper and lower GBs in
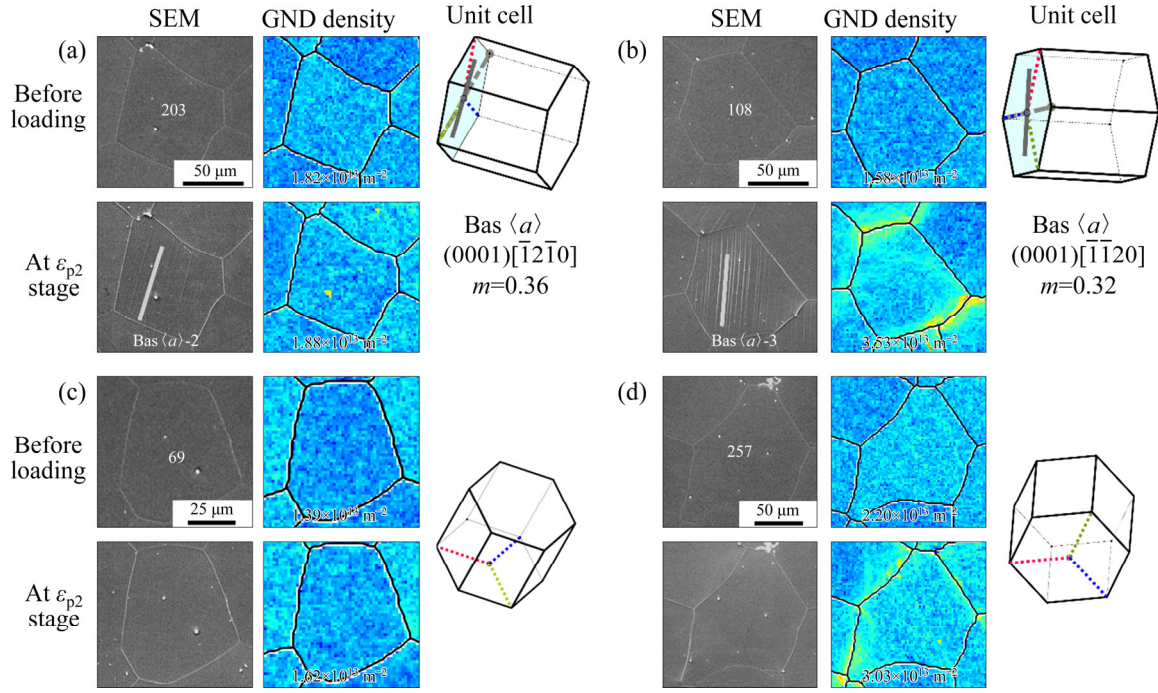
Fig. 12 Examples of GND density of grains with visible slip traces (a, b) and without visible slip traces (c, d): (a) Grain 203; (b) Grain 108; (c) Grain 69; (d) Grain 257

Grain 108 (Fig. 12(b)), whose slip system was also identified as Bas $\langle a \rangle$ ($(0001)[\bar{1}\bar{1}20]$) slip, but high and inhomogeneous GND density was observed near these GBs. As for the grains without slip traces, the GND density of Grain 69 was relatively low and uniform before loading and after deformation (Fig. 12(c)), while the extremely high GND density was distributed near GB of the Grain 257 (Fig. 12(d)). In summary, the plastic heterogeneity (the magnitude/distribution of GND density) of a grain was independent of the observed slip traces.

To further analyze the correlation between the observed slip traces and plastic heterogeneity from a statistical viewpoint, the increasing rates of GOS and gGND density [46] are calculated as follows:

$$G_{GOS}^{k} = \frac{GOS_{P2}^{k} - GOS_{P0}^{k}}{GOS_{P0}^{k}} \qquad (2)$$

$$G_{gGND}^{k} = \frac{gGND_{P2}^{k} - gGND_{P0}^{k}}{gGND_{P0}^{k}} \qquad (3)$$

where G_{GOS}^{k} (G_{gGND}^{k}) is the increasing rate of GOS (gGND) for Grain k before loading and at ε_{p2} deformation stage, GOS_{P0}^{k} ($gGND_{P0}^{k}$) and GOS_{P2}^{k} ($gGND_{P2}^{k}$) are the GOS (gGND) for Grain k before loading and at ε_{p2} deformation stage, respectively.

Figure 13 shows the G_{GOS}^{k} and G_{gGND}^{k}, where grains with and without slip traces were distinguished by different colors. For GOS, no matter whether the slip trace was observed, its G_{GOS}^{k} can be large or small. In addition, the average G_{GOS}^{k} of the grains with slip trace was slightly larger than that of the grains without slip trace. For G_{gGND}^{k}, a similar trend was also found, except that the discrepancy between the grains with and without slip traces was relatively small. In a word, whether slip traces were observed in grain did not affect the increasing rate of IGM/GND density caused by deformation. In addition, Fig. 13 also shows that there was no obvious correlation between the increasing rate of IGM/GND density and the grain size.

According to the above analysis, there was no obvious relationship between the magnitude/distribution of IGM (GND density) and whether the slip trace was observed. Interestingly, similar results were also reported [29,53]. In the Mg−5.4Gd−4.8Y−1.5Zn alloy [29], based on high angular resolution EBSD analysis, unlike the distribution of the observed slip traces in a grain, the high GND density only existed in a part area of the interior of the grain. In addition, some researchers [53] have found that the spatial

correlation between local plastic strain and local misorientation was weak in the Ni-based superalloy by using EBSD and high resolution DIC analysis. In fact, the relationship between local plastic strain and local misorientation was complicated, and further work was needed.

THOOL et al [58] found that grain orientation was related to deformation inhomogeneity (using a research method combining experiment and modeling), during the study of zirconium alloys. To explore the influence of grain orientation on inhomogeneous plastic deformation, the relationship between GOS/gGND density and $m_{max}^{Bas\langle a\rangle}$ / $m_{max}^{Pri\langle a\rangle}$ / $m_{max}^{Pyr\,II\langle c+a\rangle}$ / $m_{max}^{Pyr\,I\langle a\rangle}$ was studied from a statistical perspective. As shown in

Fig. 14(a), as $m_{max}^{Bas\langle a\rangle}$ was changed from 0 to 0.5, most of GOS values were between 0° and 1°, and showed the characteristics of random distribution. Other slip modes were similar to the Bas $\langle a\rangle$ slip. This indicated that there was no obvious correlation between GOS and m_{max} (particular slip mode). The gGND density also showed no obvious correlation with m_{max} (particular slip mode) (Fig. 14(b)). Moreover, compared with the orientation of the grains themselves, the discrepancy in orientation between adjacent grains had a closer relationship with the plastic heterogeneity, which has been reported in Mg−11Y−5Gd−2Zn−0.5Zr alloy [46], Mg−1Zn−0.5Nd alloy [32] and interstitial free steel [39].
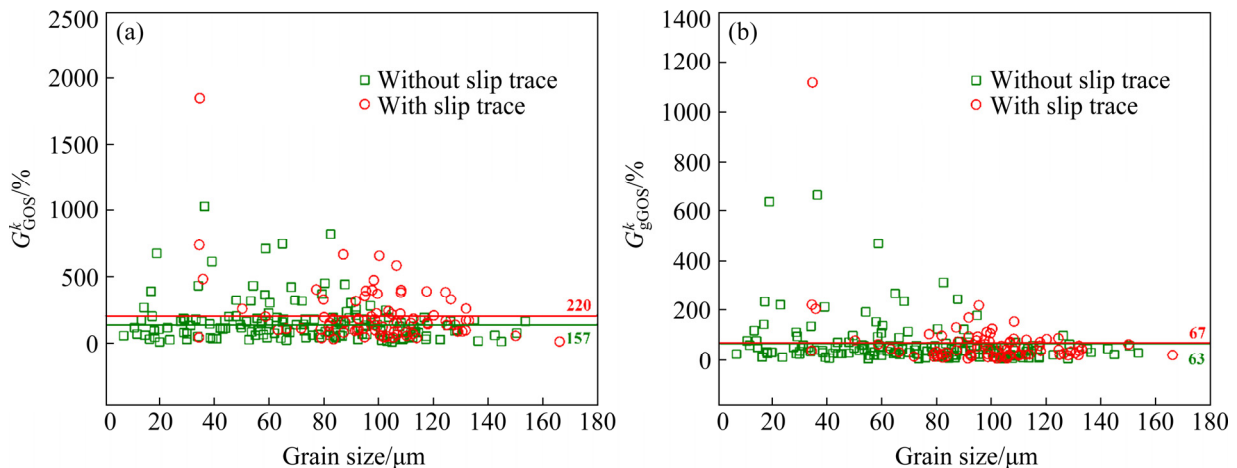

Fig. 13 Comparison of increasing rate of GOS (a) and gGND (b) between grains with and without visible slip traces after deformation (The horizontal lines and numbers represent the corresponding mean values)
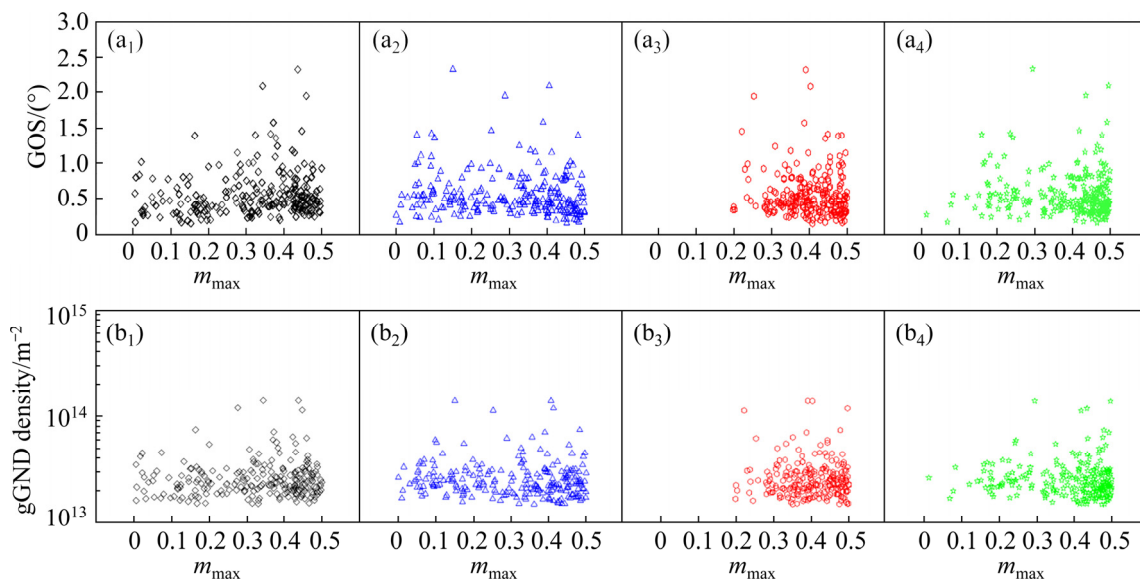

Fig. 14 Relationship between m_{max} for particular slip mode and GOS (a), and gGND density (b): (a$_1$, b$_1$) Bas $\langle a\rangle$ slip; (a$_2$, b$_2$) Pri $\langle a\rangle$ slip; (a$_3$, b$_3$) Pyr II $\langle a+c\rangle$; (a$_4$, b$_4$) Pyr I $\langle a\rangle$ slip

Figure 15 shows the GB with high GND density, the corresponding GBMA and m_{max} of particular slip mode. In Fig. 15(a), the high GND density was distributed between Grains 1 and 2 (represented as 1−2 GB), and GBMA was large ($\geq 60°$), as indicated by the arrow. Similarly, the GBMA of 3−4 GB was also very large ($\geq 60°$) and also exhibited high GND density (Fig. 15(b)), and there was a large discrepancy (>0.1) in $m_{max}^{Bas \langle a \rangle}$ / $m_{max}^{Pri \langle a \rangle}$ / $m_{max}^{Pyr I \langle a \rangle}$. Even for GBs with GBMA ($<60°$), the discrepancy of $m_{max}^{Bas \langle a \rangle}$ / $m_{max}^{Pri \langle a \rangle}$ was huge, as shown in Fig. 15(c). The arrow in the figure indicated that the GBMA (m_{max}) between them was large (the discrepancy was large). More examples showing similar trends were provided in Figs. 15(d−h).

Based on the above analysis, all of the GBs exhibiting extremely large GND density were analyzed. For most of these GBs, at least one of the following conditions was satisfied: (1) large GBMA, and (2) larger deviation of m_{max} for a particular slip mode between neighboring grains. With the similar regularity, in our previous study on WGZ1152 alloy, we found that the high GBMA/
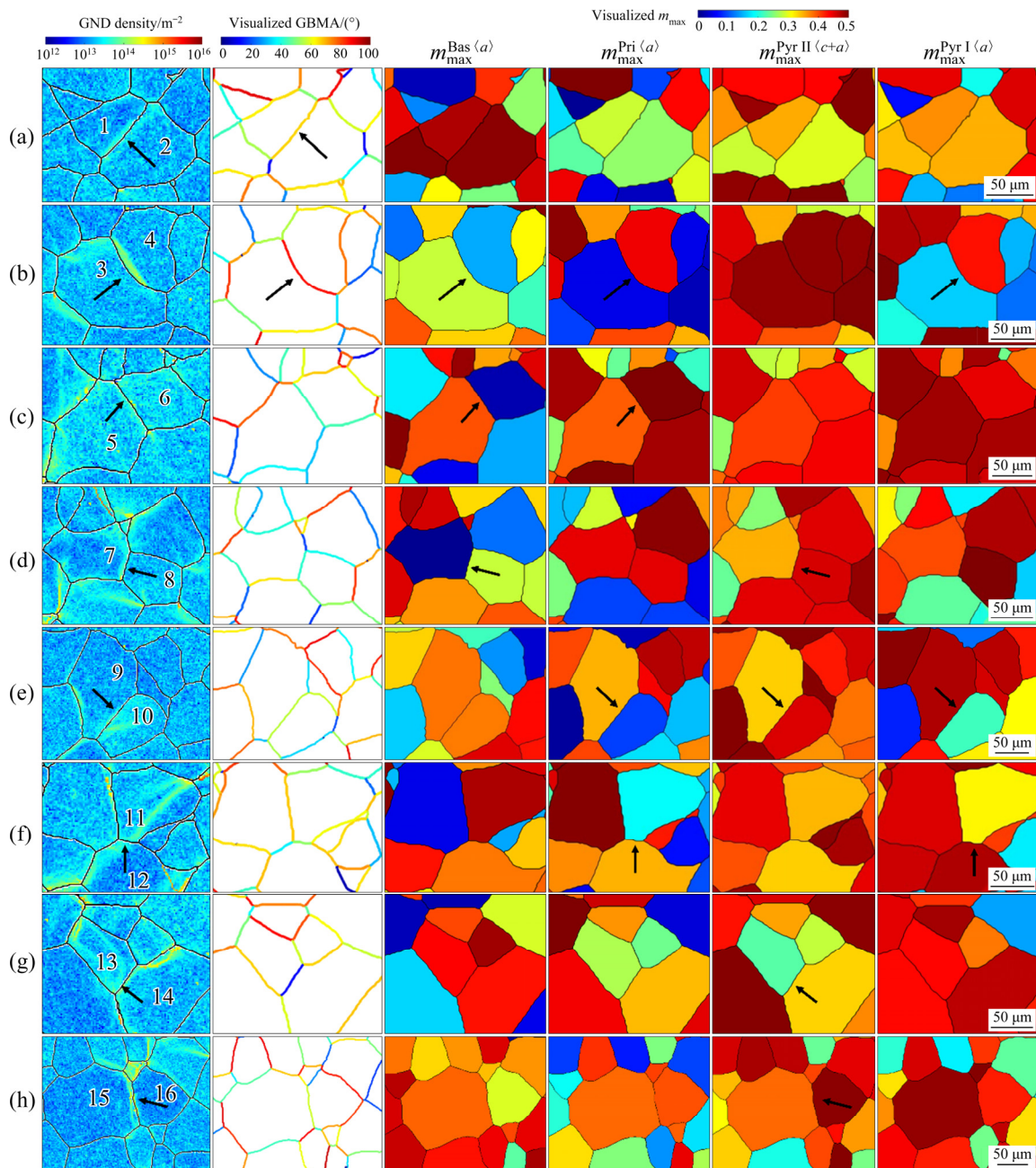

Fig. 15 Examples revealing relationship between high GND density near grain boundary and orientation discrepancy of neighborhood grains

large $m_{\max}^{\mathrm{Bas}\langle a\rangle}$ discrepancy between adjacent grains is related to the high GND density of GB [46]. This was also consistent with previous studies by other groups. For example, based on Schmid factor analysis, MARTIN et al [32,35] found that for Mg−1.3Zn−0.25Zr−0.2Nd and Mg−1Zn−0.5Nd alloys, the orientation of adjacent grains played a key role in the local strain distribution.

5 Conclusions

(1) At $\varepsilon_{\mathrm{p2}}$ deformation stage, the dominant slip mode was Bas $\langle a\rangle$ slip (73.3%). The activation of the other slip modes were 15.8% Pri $\langle a\rangle$ slip, 6.9% Pyr II $\langle c+a\rangle$ slip, and 4% Pyr I $\langle a\rangle$ slip. No twins were clearly observed. Among them, for Bas $\langle a\rangle$ slip and Pri $\langle a\rangle$ slip, the frequencies of $m>0.3$ are 68.9% and 88.0%, respectively. However, the m distribution of Pyr II $\langle c+a\rangle$ slip and Pyr I $\langle a\rangle$ slip was random.

(2) The IGM and GND density were small and exhibited a uniform distribution for most grains before deformation. However, the magnitude of IGM/GND density was greatly increased, and the distribution of IGM and GND density became more inhomogeneous, especially at the vicinity of GBs.

(3) The IGM and GND density (magnitude/ distribution) were irrelative with the visibility of slip traces and the grain size. There was no obvious correlation between GOS and $m_{\max}$ (particular slip mode).

(4) For most of the GBs exhibiting extremely large GND density, at least one of the following conditions was satisfied: large GBMA and/or large deviation of $m_{\max}$ for a particular slip mode between neighboring grains.

References

[1] MORDIKE B L, EBERT T. Magnesium: Properties− applications−potential [J]. Materials Science and Engineering A, 2001, 302: 37−45.

[2] POLMEAR I J. Magnesium alloys and applications [J]. Materials Science and Technology, 2013, 10(1): 1−16.

[3] CAO Fu-yong, ZHANG Jing, LI Ke-ke, SONG Guang-ling. Influence of heat treatment on corrosion behavior of hot rolled Mg5Gd alloys [J]. Transactions of Nonferrous Metals Society of China, 2021, 31(4): 939−951.

[4] LI Zi-han, ZHOU Guo-wei, LI Da-yong, WANG Hua-miao, TANG Wei-qin, PENG Ying-hong, ZUROB H S, WU Pei-dong. Crystal plasticity based modeling of grain boundary sliding in magnesium alloy AZ31B sheet [J]. Transactions of Nonferrous Metals Society of China, 2021, 31(1): 138−155.

[5] FENG Li, ZHANG You-wei, WEN Chen, LI Si-zhen, LI Jia-feng, CHENG De, BAI Jing-ying, CUI Qing-xin, ZHANG Li-gong. Effect of initial deposition behavior on properties of electroless Ni−P coating on ZK60 and ME20 magnesium alloys [J]. Transactions of Nonferrous Metals Society of China, 2021, 31(8): 2307−2322.

[6] HAN Ting-zhuang, HUANG Guang-sheng, MA Li-feng, WANG Guan-gang, WANG Li-fei, PAN Fu-sheng. Evolution of microstructure and mechanical properties of AZ31 Mg alloy sheets processed by accumulated extrusion bonding with different relative orientation [J]. Journal of Alloys and Compounds, 2019, 784: 584−591.

[7] TANG Y T, ZHANG C, REN L B, YANG W, YIN D D, HUANG G H, ZHOU H, ZHANG Y B. Effects of Y content and temperature on the damping capacity of extruded Mg−Y sheets [J]. Journal of Magnesium and Alloys, 2019, 7(3): 522−528.

[8] FAN Ling-ling, ZHOU Ming-yang, GUO Yang-yang, ZHANG Yu-wen-xi, QUAN Gao-feng. Effect of ECAP process on liquid distribution of AZ80M alloy during semi-solid isothermal heat treatment [J]. Transactions of Nonferrous Metals Society of China, 2021, 31(6): 1599−1611.

[9] PENG Yong-gang, DU Zhi-wei, LIU Wei, LI Yong-jun, LI Ting, HAN Xiao-lei, MA Ming-long, PANG Zheng, YUAN Jia-wei, SHI Guo-liang. Evolution of precipitates in Mg−7Gd−3Y−1Nd−1Zn−0.5Zr alloy with fine plate-like 14H-LPSO structures aged at 240 °C [J]. Transactions of Nonferrous Metals Society of China, 2020, 30(6): 1500−1510.

[10] ANSARI N, SARVESHA R, LEE S Y, SINGH S S, JAIN J. Influence of yttrium addition on recrystallization, texture and mechanical properties of binary Mg−Y alloys [J]. Materials Science and Engineering A, 2020, 793: 139856.

[11] GAO L, CHEN R S, HAN E H. Effects of rare-earth elements Gd and Y on the solid solution strengthening of Mg

alloys [J]. Journal of Alloys and Compounds, 2009, 481: 379−384.

[12] HE S M, ZENG X Q, PENG L M, GAO X, NIE J F, DING W J. Microstructure and strengthening mechanism of high strength Mg–10Gd–2Y–0.5Zr alloy [J]. Journal of Alloys and Compounds, 2007, 427: 316−323.

[13] SUN K X, ZENG Y, YIN D D, GAO F, LONG L J, QIAN X Y, WAN Y J, QUAN G F, JIANG B. Quantitative study on slip/twinning activity and theoretical critical shear strength of Mg alloy with Y addition [J]. Materials Science and Engineering A, 2020, 792: 139801.

[14] JANIK V, YIN D D, WANG Q D, HE S M, CHEN C J, CHEN Z, BOEHLERT C J. The elevated-temperature mechanical behavior of peak-aged Mg–10Gd–3Y–0.4Zr Alloy [J]. Materials Science and Engineering A, 2011, 528: 3105−3112.

[15] WANG H, WANG Q D, BOEHLERT C J, YIN D D, YUAN J. Tensile and compressive creep behavior of extruded Mg–10Gd–3Y–0.5Zr (wt.%) alloy [J]. Materials Characterization, 2015, 99: 25−37.

[16] WANG H, WANG Q D, BOEHLERT C J, YANG J, YIN D D, YUAN J, DING W J. The impression creep behavior and microstructure evolution of cast and cast-then-extruded Mg−10Gd−3Y−0.5Zr (wt%) [J]. Materials Science and Engineering A, 2016, 649: 313−324.

[17] CEPEDA-JIMÉNEZ C M, PRADO-MARTÍNEZ C, PÉREZ-PRADO M T. Understanding the high temperature reversed yield asymmetry in a Mg-rare earth alloy by slip trace analysis [J]. Acta Materialia, 2018, 145: 264−277.

[18] WU Z, AHMAD R, YIN B, SANDLOBES S, CURTIN W A. Mechanistic origin and prediction of enhanced ductility in magnesium alloys [J]. Science, 2018, 359(6374): 447−452.

[19] WANG F, SANDLÖBES S, DIEHL M, SHARMA L, ROTERS F, RAABE D. In situ observation of collective grain-scale mechanics in Mg and Mg–rare earth alloys [J]. Acta Materialia, 2014, 80: 77−93.

[20] WEI Kang, XIAO Li-rong, GAO Bo, LI Lei, LIU Yi, DING Zhi-gang, LIU Wei, ZHOU Hao, ZHAO Yong-hao. Enhancing the strain hardening and ductility of Mg−Y alloy by introducing stacking faults [J]. Journal of Magnesium and Alloys, 2020, 8(4): 1221−1227.

[21] YIN D D, WANG Q D, BOEHLERT C J, CHEN Z, LI H M, MISHRA R K, CHAKKEDATH A. In-situ study of the tensile deformation and fracture modes in peak-aged cast Mg−11Y−5Gd−2Zn−0.5Zr (weight percent) [J]. Metallurgy and Materials Transactions A, 2016, 47(12): 6438−6452.

[22] TAYLOR S, WEST G D, MOGIRE E, TANG F, KOTADIA H R. Superplastic forming characteristics of AZ41 magnesium alloy [J]. Transactions of Nonferrous Metals Society of China, 2021, 31(3): 648−654.

[23] AGNEW S R, MULAY R P, POLESAK F J, CALHOUN C A, BHATTACHARYYA J J, CLAUSEN B. In situ neutron diffraction and polycrystal plasticity modeling of a Mg−Y−Nd−Zr alloy: Effects of precipitation on individual deformation mechanisms [J]. Acta Materialia, 2013, 61: 3769−3780.

[24] HU W W, YANG Z Q, YE H Q. ⟨c+a⟩ dislocations and their interactions with other crystal defects in a Mg alloy [J]. Acta Materialia, 2017, 124: 372−382.

[25] WANG H, BOEHLERT C J, WANG Q D, YIN D D, DING W J. In-situ analysis of the tensile deformation modes and anisotropy of extruded Mg−10Gd−3Y−0.5Zr (wt.%) at elevated temperatures [J]. International Journal of Plasticity, 2016, 84: 255−276.

[26] WANG H, BOEHLERT C J, WANG Q D, YIN D D, DING W J. In-situ analysis of the slip activity during tensile deformation of cast and extruded Mg−10Gd−3Y−0.5Zr (wt.%) at 250 °C [J]. Materials Characterization, 2016, 116: 8−17.

[27] XIAO Lei, YANG Guang-yu, QIN He, MA Jia-qi, JIE Wan-qi. Asymmetric tension−compression mechanical behavior of the as-cast Mg−4.58Zn−2.6Gd−0.16Zr alloy [J]. Materials Science and Engineering A, 2021, 801: 140439.

[28] LU J W, YIN D D, REN L B, QUAN G F. Tensile and compressive deformation behavior of peak-aged cast Mg−11Y−5Gd−2Zn−0.5Zr (wt.%) alloy at elevated temperatures [J]. Journal of Materials Science, 2016, 51(23): 10464−10477.

[29] JIANG Shao-song, JIA Yong, WANG Xiao-jun, JIANG Ju-fu. Precise measurement of strain accommodation in a Mg−Gd−Y−Zn alloy using cross-correlation-based high resolution EBSD [J]. Materials Characterization, 2020, 165: 110384.

[30] GITHENS A, GANESAN S, CHEN Z, ALLISON J, SUNDARARAGHAVAN V, DALY S. Characterizing microscale deformation mechanisms and macroscopic tensile properties of a high strength magnesium rare-earth alloy: A combined experimental and crystal plasticity approach [J]. Acta Materialia, 2020, 186: 77−94.

[31] di GIOACCHINO F, da FONSECA J Q. An experimental study of the polycrystalline plasticity of austenitic stainless steel [J]. International Journal of Plasticity, 2015, 74: 92−109.

[32] MARTIN G, SINCLAIR C W, SCHMITT J H. Plastic strain heterogeneities in an Mg−1Zn−0.5Nd alloy [J]. Scripta Materialia, 2013, 68: 695−698.

[33] CHARPAGNE M A, STINVILLE J C, CALLAHAN P G, TEXIER D, CHEN Z, VILLECHAISE P, VALLE V, POLLOCK T M. Automated and quantitative analysis of plastic strain localization via multi-modal data recombination [J]. Materials Characterization, 2020, 163: 110245.

[34] KAMAYA M. Assessment of local deformation using EBSD: Quantification of local damage at grain boundaries [J]. Materials Characterization, 2012, 66: 56−67.

[35] MARTIN G, SINCLAIR C W, LEBENSOHN R A. Microscale plastic strain heterogeneity in slip dominated deformation of magnesium alloy containing rare earth [J]. Materials Science and Engineering A, 2014, 603: 37−51.

[36] CHAI Y Q, BOEHLERT C J, WAN Y F, HUANG G H, ZHOU H, ZHENG J, WANG Q D, YIN D D. Anomalous tension twinning activity in extruded mg sheet during hard-orientation loading at room temperature [J].

Metallurgical and Materials Transactions A, 2021, 52(2): 449−456.

[37] WU Hao, FAN Guo-hua. An overview of tailoring strain delocalization for strength-ductility synergy [J]. Progress in Materials Science, 2020, 113: 100675.

[38] MURÁNSKY O, BALOGH L, TRAN M, HAMELIN C-J, PARK J S, DAYMOND M R. On the measurement of dislocations and dislocation substructures using EBSD and HRSD techniques [J]. Acta Materialia, 2019, 175: 297−313.

[39] ALLAIN-BONASSO N, WAGNER F, BERBENNI S, FIELD D P. A study of the heterogeneity of plastic deformation in IF steel by EBSD [J]. Materials Science and Engineering A, 2012, 548: 56−63.

[40] ZHOU Guo-wei, JAIN M K, WU Pei-dong, SHAO Yi-chuan, LI Da-yong, PENG Ying-hong. Experiment and crystal plasticity analysis on plastic deformation of AZ31B Mg alloy sheet under intermediate temperatures: How deformation mechanisms evolve [J]. International Journal of Plasticity, 2016, 79: 19−47.

[41] YIN D D, BOEHLERT C J, LONG L J, HUANG G H, ZHOU H, ZHENG J, WANG Q D. Tension-compression asymmetry and the underlying slip/twinning activity in extruded Mg–Y sheets [J]. International Journal of Plasticity, 2021, 136: 102878.

[42] KALIDINDI S R, ABUSAFIEH A, EL-DANAF E. Accurate characterization of machine compliance for simple compression testing [J]. Experimental Mechanics, 1997, 37(2): 210−215.

[43] KULA A, JIA X, MISHRA R K, NIEWCZAS M. Flow stress and work hardening of Mg–Y alloys [J]. International Journal of Plasticity, 2017, 92: 96−121.

[44] HIELSCHER R, SILBERMANN C B, SCHMIDL E, IHLEMANN J. Denoising of crystal orientation maps [J]. Journal of Applied Crystallography, 2019, 52(5): 984−996.

[45] BACHMANN F, HIELSCHER R, SCHAEBEN H. Texture analysis with MTEX–Free and open source software toolbox [J]. SSP, 2010, 160: 63−68.

[46] NI R, MA S J, LONG L J, ZHENG J, ZHOU H, WANG Q D, YIN D D. Effects of precipitate on the slip activity and plastic heterogeneity of Mg−11Y−5Gd−2Zn−0.5Zr (wt.%) during room temperature compression [J]. Materials Science and Engineering A, 2021, 804: 140738.

[47] DENG Y C, HUANG Z J, LI T J, YIN D D, ZHENG J. Quantitative investigation on the slip/twinning activity and cracking behavior during low-cycle fatigue of an extruded Mg−3Y sheet [J]. Metallurgical and Materials Transactions A, 2021, 52(1): 332.

[48] LONG L J, HUANG G H, YIN D D, JI B, ZHOU H, WANG Q D. Effects of Y on the deformation mechanisms of extruded Mg−Y sheets during room-temperature compression [J]. Metallurgical and Materials Transactions A, 2020, 51(6): 2738−2751.

[49] EL-DASHER B S, ADAMS B L, ROLLETT A D. Viewpoint: Experimental recovery of geometrically necessary dislocation density in polycrystals [J]. Scripta Materialia, 2003, 48: 141−145.

[50] PANTLEON W. Resolving the geometrically necessary dislocation content by conventional electron backscatter diffraction [J]. Scripta Materialia, 2008, 58: 994−997.

[51] WU W X, JIN L, DONG J, DING W J. Deformation behavior and texture evolution in an extruded Mg−1Gd alloy during uniaxial compression [J]. Materials Science and Engineering A, 2014, 593: 48−54.

[52] BOEHLERT C J, CHEN Z, GUTIÉRREZ-URRUTIA I, LLORCA J, PÉREZ-PRADO M T. In situ analysis of the tensile and tensile-creep deformation mechanisms in rolled AZ31 [J]. Acta Materialia, 2012, 60: 1889−1904.

[53] HARTE A, ATKINSON M, PREUSS M, QUINTA DA FONSECA J. A statistical study of the relationship between plastic strain and lattice misorientation on the surface of a deformed Ni-based superalloy [J]. Acta Materialia, 2020, 195: 555−570.

[54] TANG Ao, LIU Hai-ting, LIU Gui-sen, ZHONG Yong, WANG Li, LU Qi, WANG J, SHEN Yao. Lognormal distribution of local strain: A universal law of plastic deformation in material [J]. Physical Review Letters, 2020, 124(15): 155501.

[55] BHATTACHARYYA J J, WANG F, STANFORD N, AGNEW S R. Slip mode dependency of dislocation shearing and looping of precipitates in Mg alloy WE43 [J]. Acta Materialia, 2018, 146: 55−62.

[56] NIE Jian-feng. Precipitation and hardening in magnesium alloys [J]. Metallurgical and Materials Transactions A, 2012, 43: 3891−3939.

[57] JAIN J, POOLE W J, SINCLAIR C W, GHARGHOURI M A. Reducing the tension–compression yield asymmetry in a Mg–8Al–0.5Zn alloy via precipitation [J]. Scripta Materialia, 2010, 62: 301−304.

[58] THOOL K, PATRA A, FULLWOOD D, KRISHNA K V M, SRIVASTAVA D, SAMAJDAR I. The role of crystallographic orientations on heterogeneous deformation in a zirconium alloy: A combined experimental and modeling study [J]. International Journal of Plasticity, 2020, 133: 102785.

Mg−10Gd−3Y−0.5Zr 合金在压缩变形中的
滑移系激活规律和塑性变形不均匀性

江志伟 [1]，尹冬弟 [1]，万有富 [1]，倪 然 [1]，周 浩 [2]，郑 江 [3]，王渠东 [4]

1. 西南交通大学 材料科学与工程学院 材料先进技术教育部重点实验室，成都 610031；
2. 南京理工大学 材料科学与工程学院 纳米异构材料中心，南京 210094；
3. 重庆大学 材料科学与工程学院 教育部轻合金材料国际合作联合实验室
沈阳材料科学国家研究中心，重庆 400044；
4. 上海交通大学 材料科学与工程学院 轻合金精密成型国家工程研究中心，上海 200240

摘 要：为了定量和统计地了解高性能铸造 Mg−10Gd−3Y−0.5Zr(质量分数，%，GW103)合金在室温单轴压缩变形中滑移系的激活规律和塑性变形不均匀性，对时效状态的该合金进行详细的滑移迹线分析和基于取向差的电子背散射衍射(EBSD)分析。在 2%塑性应变后，根据鉴别的滑移迹线的相对比例，激活的滑移模式首先为基面⟨a⟩滑移(73.3%)，其次是柱面⟨a⟩滑移(15.8%)，然后是二级角锥面⟨c+a⟩滑移(6.9%)，最后是一级角锥面⟨a⟩滑移(4%)。尽管大多数激活的滑移系表现出较大的施密特因子(m)值(>0.3)，但值得注意的是，一些硬取向(m<0.1)的滑移系也被激活。对于大多数表现出极大几何必需位错(GND)密度的晶界，至少满足以下条件之一：晶界取向差角(GBMA)较大；相邻晶粒间特定滑移模式 m_{max} 之差较大。晶粒的塑性变形不均匀性(GND 密度的大小/分布)与是否能观察到滑移迹线无关。晶内取向分布(GOS)和/或平均 GND 密度与 m_{max} (对于特定滑移模式)没有明显的相关性。
关键词：稀土镁合金；滑移系激活规律；滑移迹线分析；塑性变形不均匀性；几何必需位错密度

(Edited by Bing YANG)